Research article

FeMn and FeMnAg biodegradable alloys: An *in vitro* and *in vivo* investigation

Luke Saliba [a,f,1], Keith Sammut [a,f,1], Christabelle Tonna [b], Foteini Pavli [c], Vasilis Valdramidis [c], Ray Gatt [a], Ryan Giordmaina [a], Liberato Camilleri [d], William Atanasio [e], Joseph Buhagiar [b,*], Pierre Schembri Wismayer [f]

[a] *Department of Trauma, Orthopaedics and Sports Medicine, Mater Dei Hospital, Msida, MSD 2090, Malta*
[b] *Department of Metallurgy and Materials Engineering, University of Malta, Msida, MSD 2080, Malta*
[c] *Department of Food Sciences and Nutrition, University of Malta, Msida, MSD 2080, Malta*
[d] *Department of Statistics and Operations Research, University of Malta, Msida, MSD 2080, Malta*
[e] *Mortuary and Anatomic Pathology Department, Mater Dei Hospital, Msida, MSD 2090, Malta*
[f] *Department of Anatomy, University of Malta, Msida, MSD 2080, Malta*

ABSTRACT

Iron-based biodegradable metal bone graft substitutes are in their infancy but promise to fill bone defects that arise after incidents such as trauma and revision arthroplasty surgery. Before clinical use however, a better understanding of their *in vivo* biodegradability, potential cytotoxicity and biocompatibility is required. In addition, these implants must ideally be able to resist infection, a complication of any implant surgery. In this study there was significant *in vitro* cytotoxicity caused by pure Fe, FeMn, FeMn1Ag and FeMn5Ag on both human foetal osteoblast (hFOB) and mouse pre-osteoblast (MC3T3-E1) cell lines. *In vivo* experiments on the other hand showed no signs of ill-effect on GAERS rats with the implanted FeMn, FeMn1Ag and FeMn5Ag pins being removed largely uncorroded. All Fe-alloys showed anti-bacterial performance but most markedly so in the Ag-containing alloys, there is significant bacterial resistance *in vitro*.

1. Introduction

Permanent implants and bone grafts have been used successfully to repair bone defects for a long time. However, they carry with them several limitations, for instance patients requiring revision surgery, inadequate material properties leading to stress shielding and osteoporosis, and in the case of paediatric patients restricted bone development. Bone graft substitutes are an evolving area of research in modern orthopaedic practice [1–3]. Metals, in particular magnesium alloys have been studied extensively in this regard, but this material faces challenges with regards to both its structural properties and corrosion resistance, hence being unable to offer the support required in load-bearing applications [4–6].

Other materials have since also been studied, Fe-based alloys being amongst those that have shown promise, not least for their potential to be used in load-bearing orthopaedic applications. Pure Fe corrodes at a rate which is too slow to allow it to fulfil its aim as a biodegradable bone graft substitute; *in vivo* implants being left largely intact and uncorroded after a period of 1 year or more, this likely

---

largely contributing to its low cytotoxicity [7–11]. As a solution to this slow corrosion rate, several potential alloying elements have been proposed, including manganese. When Mn is alloyed with Fe in particular proportions, the resultant alloy exhibits similarly favourable mechanical properties as pure Fe, lending well to the load-bearing applications for which the final implant is intended and also removing its magnetism, rendering such implants potentially compatible with modern imaging techniques such as magnetic resonance imaging (MRI) [12,13]. In addition, while some contradictory results exist, FeMn has largely been shown to corrode more rapidly *in vitro* than does pure Fe, especially if combined with other elements such as silver, which tends to result in accelerated degradation due to microgalvanic corrosion [12,14–20].

As a potential consequence of new alloying elements however comes the fear of cytotoxicity. Mn in particular, though important for normal human physiology and found naturally in trace amounts in the body, has the potential to cause significant systemic toxicity if present in supra-physiological quantities [21,22]. At a cellular level some evidence however exists to support a good *in vitro* cytotoxicity profile of alloys such as FeMn [12,13,23–26]. The majority of this evidence comes from studies employing indirect or extract-based cytotoxicity testing methods which poorly mimic an *in vivo* situation where the implant is expected and needed to continue corroding after implantation. There is very little with regards to direct contact testing with results showing a less favourable cytotoxicity profile [27]. *In vivo* evidence is similarly scant with evidence so far suggesting good biocompatibility, but with corrosion rates similar to Fe and therefore too slow [24].

For this reason, interest once again began to shift towards the identification of new elements which would increase the corrosion rate of implants formed from FeMn-X alloys, Pd being one such element [28]. Another suggested element has been Ag, which while maintaining the favourable structural characteristics of FeMn, has been shown to increase degradation rates through microgalvanic corrosion when added in excess of 1 wt% [14,16,29,30]. Most recently, work such as that by Dargusch *et al.*, 2021, reported on the increased corrosion rate of materials such as FeMn1Ag when implanted *in vivo* [31], building on already available evidence delineating the increased but still slow corrosion rate of other materials such as FeMnPd [32]. New promise therefore lies in such novel alloys to provide a solution to this problem, but evidence here is still severely lacking.

The implantation of any prosthetic material into the human body carries with it a risk of periprosthetic infection. Periprosthetic infections of such a nature pose great treatment challenges, as they rarely ever respond completely to antibiotics alone [33–35], and usually necessitate removal of the implant for effective management. This is due to the ability of bacteria to form biofilms on implant surfaces – aggregates of bacterial cells securely embedded within an extracellular polymeric substance (EPS) and firmly attached to the underlying substratum [33–35]. In the case of temporary devices such as urinary catheters and central venous catheters, these may usually be changed with ease. However, in the case of orthopaedic implants, such as in arthroplasty, this usually necessitates complex, staged revision surgeries that carry a significant risk of morbidity and mortality, potentially costing over 20 times the index operation [35–37] and are associated with a 15–25% rate of re-infection [38–41], often necessitating further intervention. It is therefore of utmost importance that great care is taken to prevent the onset of such infections, with a multimodal strategy of careful, sterile implantation technique, prophylactic antibiotics, correct soft-tissue handling and antibiotic-impregnated implant materials being employed.

Ag has long been known to possess antibacterial activity and has been in use for millennia as a means of preserving food and water, and later on, as an antiseptic treatment for wounds. More recently, it has been shown that the use of Ag nanoparticle-lined endo-tracheal tubes in critically ill patients is associated with a lower risk of ventilator-associated pneumonia [42]. While there is extensive work on the antibacterial efficacy of Ag nanoparticle coatings in orthopaedic implants, there is substantially less on FeMnAg alloy bone scaffolds, particularly with respect to their effects on biofilm formation. One study concluded that there was no antibacterial benefit gained from the incorporation of Ag into FeMn alloys [43], whereas another observed a dose-dependent relationship between the amount of Ag incorporated with the FeMn alloy and antibacterial rates [44]. Notably, both studies assessed antibacterial rates in terms of planktonic bacterial cell populations, rather than viable, attached bacterial biomass, and varied significantly in terms of methodology. Furthermore, both studies measured antibacterial rates with respect to *Staphylococcus aureus* and *Escherichia coli*, pathogens estimated to cause just 36% of all prosthetic joint infections [45] and approximately 40% of all fracture-related infections [46].

The use of Ag is not without risks. Excessive Ag exposure manifests itself as either localised or generalised argyria – the deposition of Ag compounds such as silver sulfide and silver selenide in the skin, cornea and conjunctiva, causing an often permanent, bluish-grey discolouration [47,48]. It has also been shown to deposit in the liver and kidneys, among other viscera [49]. Additionally, exposure to Ag appears to be cumulative, with the World Health Organisation (WHO) declaring a maximum lifetime dose of 10 g of Ag as the human no-observable-adverse-effect-level [50].

This work targets a gap in current knowledge, looking both at the direct *in vitro* cytotoxicity of Fe35Mn, (Fe35Mn)1Ag and (Fe35Mn)5Ag alloys to key bone cells along with these alloys' *in vivo* biocompatibility. It also analyses the effect of FeMnAg alloys in staving off biofilm growth from a wider range of common orthopaedic pathogens.

2. Methods

2.1. Metal preparation for testing

Fe and Fe-alloy coupons were manufactured using the powder metallurgy route. Fe power (99% purity, <45 μm) supplied by US Research Nanomaterials Inc. (USA), Mn powder (99.6% purity, <10 μm) and Ag powder (99.9% purity, 4–7 μm) both supplied by Alfa Aesar (Germany) were used for this process. FeMn was manufactured to contain 65% Fe and 35% Mn by weight. FeMn1Ag and FeMn5Ag were manufactured to contain 1% and 5% by weight respectively of Ag with Fe and Mn forming 65% and 35% by weight of the remaining 99% or 95% metal. This ensured that Fe and Mn ratio was always kept at 65:35. Weighing took place with a resolution of

0.1 mg using a precision scale (Precisa, Switzerland) after which the powders were mixed using an Inversina tumbler (Bio-Components, Switzerland). In order to achieve a homogenous mixture, mixing took place over 6 h with 5 stainless steel balls, each of 10 mm diameter. The resultant powder mixtures were then weighed into 10 g $\pm$ 10 mg portions and uni-axially pressed at 442 MPa using an Instron 8802 hydraulic press (USA) in a die. Sintering took place at 1120 °C for 3 h in N_2–5H_2 flowing at 100 l/h, following a ramp rate of 180 °C/h. This yielded Fe and Fe-alloy coupons measuring 22 mm diameter and 4 mm depth. Wrought biomedical grade AISI 316LVM stainless steel (Klein SA, Switzerland) coupons with the same dimensions were used as control specimens.

Grinding of all metal coupons took place using SiC paper (Metprep, UK) to a final grit of P2500. The coupons were ultrasonicated for 5 min in 99% Isopropyl alcohol (IPA) after which they were air dried and placed under a vacuum for 2 h. For the purpose of *in vivo* biocompatibility testing, 8 sintered coupons each of FeMn, FeMn1Ag and FeMn5Ag were machined on a lathe to prepare pins of 5 mm length and 2.05 mm diameter.

Prior to testing, all pins and coupons were exposed to an acid treatment procedure to remove MnO resulting from the sintering process from the material surface. The MnO is considered as an unwanted inclusion and could have an effect on the rate of corrosion and cytotoxicity over and above the influence of the metal composition. Therefore, MnO was removed to eliminate an unwanted variability. Samples were immersed in 30 ml/coupon of 1 M HCl supplemented with 3.5 g/L hexamethylenetetramine and ultrasonicated for 5 min. All samples were then rinsed in deionised water, ultrasonicated for 5 min in IPA, dried and stored under vacuum until point of testing.

Sterilisation of all material samples, including Fe-alloy and SS316LVM coupons and Thermanox™ (Thermo Fisher Scientific™) was performed immediately prior to their use in *in vitro* tests. This was performed in a laminar flow cabinet by immersing the samples in acetone, followed by 70% isopropyl alcohol and allowing them to dry after which they were rinsed in sterile cell culture medium prior to cytotoxicity testing. For antibacterial tests, coupons were rinsed with sterile distilled water instead of cell culture medium and once again allowed to dry in a flow cabinet.

2.2. Material characterisation

For the purposes of characterisation, an extra polishing step was performed. After being ground to P2500 grit, a finer 3 µm diamond paper was used with the final polishing step being performed using an MD-Chem polishing cloth using an OP-S suspension (Struers, Denmark). Once completed, the samples were acid treated as described above in order to remove MnO from within the porous component of the coupons and examined using scanning electron microscopy (SEM, Carl Zeiss FE-SEM, Merlin Gemini II column, Germany) and EDS (AMETEK EDAX detector, USA). Although weight percent for carbon, nitrogen and oxygen were included in the measurement, one must note that the EDS technique is not appropriate for accurate measurement of light elements therefore such results must only be considered as a qualitative indication. Phase analysis of the fully prepared samples was performed using an XRD Bruker D8 Advance (USA) with a copper source (Cu-Kα, λ = 0.141 nm), equipped with a graphite monochromator. The analysis was conducted at 2θ between 30° and 100° at a rate of 0.02°/step while the sample was angularly rotating at 15°/min.

2.3. In vitro cytotoxicity testing

Cytotoxicity tests were performed using a well-established cell line of human foetal osteoblasts (hFOB 1.19, CRL-11372, ATCC®). Regular culture took place in T25 flasks (ThermoFisher Scientific™, USA) under conditions of 5% CO_2 and 34 °C. Once confluence of 80% was reached, the cells were trypsinised and a single cell suspension was prepared. The metal coupons and Thermanox™ coverslips were sterilised using 70% ethanol. After rinsing in cell culture medium, the coupons were seeded with 5 ml of cell suspension containing 30,000 cells/ml hFOBs in medium and each coupon placed in a well of a 6-well plate with 5 mls of medium in each well. Tests were performed over a 4-day period. A total of 3 replicates of each condition (Fe, FeMn, FeMn1Ag and FeMn5Ag coupons) were tested on each day of testing along with controls of stainless steel 316LVM, Thermanox™ and medium alone. Stainless steel 316LVM was used because this material is used in daily orthopaedic practice, a large proportion of implants being manufactured from this material, none of which being expected to show any significant corrosion over time. On days 1, 2 and 4, the cells were removed from the coupons/Thermanox™ by lysis and a 1:30 dilution of this solution was used to perform cell viability testing using CellTiter-Glo® luminescent assay (Promega®), in line with the recommended testing protocol set out by the manufacturer. This luminescent signal, depending on the amount of ATP present was read by a microplate reader (Tecan®, USA) in opaque-walled 96-well plates.

A replicate experiment was secondarily performed with a cell line of mouse pre-osteoblasts (MC3T3-E1 Subclone 4, CRL-2593, ATCC®) seeded onto pre-corroded coupons as well as freshly-ground, uncorroded coupons. Several studies have indicated that the corrosion rate of Fe-based alloys tends to decrease with time as the initially high release of metal ions is retarded by accumulated corrosion products on the metal surface [51,52]. With pre-corroded coupons, this was expected to have a direct impact of measured cytotoxicity due to potentially lowered ion release rates. In addition, in order to relate *in vitro* tests more closely to *in vivo* tests, a mouse pre-osteoblast cell line was used as detailed above.

Four coupons of Fe, FeMn, FeMn1Ag, FeMn5Ag and 2 coupons of SS316LVM were sterilised and pre-corroded for a total of 3 days in culture medium at 37 °C and with 5% CO_2. These coupons were then rinsed with fresh medium and three transferred into fresh 6-well plates and seeded with cells together with 1 uncorroded coupon of each Fe-alloy. This uncorroded coupon was prepared as for the hFOB cytotoxicity tests. MC3T3-E1 cells were then seeded at 15,000 cells/ml in 5 ml of cell suspension/well. CellTiter-Glo® testing was then performed as for the hFOB cytotoxicity tests.

The final, fourth coupon of each material was transferred into a separate 6-well plate along with a SS316LVM coupon and these also seeded with MC3T3-E1 cells, these to be examined using SEM. On each test day, under a fume cupboard, each coupon was rinsed first

with phosphate buffered solution (PBS) and then immersed in a fixing solution containing 10% v/v of 25% Glutaraldehyde, 50% v/v of 0.5 M sodium cacodylate buffer pH 7.3 and 40% v/v distilled water. This was performed for 10 min after which the solution was replaced with 0.1 M sodium cacodylate buffer pH 7.3. After a further 10 min, the solution was removed and 25% ethanol added for 10 min. Ethanol at 50%, 60%, 70%, 80%, 90% and 100% were then each added for 10 min in order to dehydrate any cells present on the coupon surface. Hexamethyldisilizane was finally added for 10 min, removed and the coupons allowed to dry for 1 h. The samples were gold-sputtered for 30 s using a sputter coater (Agar, USA) and examined using SEM.

2.4. In vitro antibacterial testing

Stock cultures of *Staphylococcus aureus* (NCTC 6571), *Staphylococcus epidermidis* (NCTC 10519) (as a coagulase-negative staphylococcus model organism), *Streptococcus agalactiae* (NCTC 11247) (as a Lancefield Group B model organism) and *Escherichia coli* (NCTC 12241) (as a gram-negative model organism) were grown from freeze-dried strains, obtained from Culture Collections, Public Health England, according to NCTC guidelines, and streak-plated on Tryptic Soy Agar (TSA) plates (Scharlab, Spain). A first inoculation was then performed by picking a single colony using a sterile loop and transferring it to a test tube containing 10 mL of Tryptic Soy Broth (TSB) without Dextrose (Scharlab, Spain). This mixture was then vortexed thoroughly to ensure adequate dispersal of the biomass within the solution, and subsequently incubated for 24 h at 37 °C.

Sterilised FeMn, FeMn1Ag and FeMn5Ag coupons were then placed into centrifuge tubes containing TSB (without dextrose) and inoculated with each bacterial strain in order to obtain a final inoculum concentration of 5 log (CFU/mL). Following inoculation, the tubes were incubated at 37 °C for 24 h to enable bacterial proliferation and biofilm formation.

The inoculated coupons were removed after 24 h, rinsed 3 times with 10 mL Ringer's Solution (ThermoFisher Scientific™, USA) each, in order to remove any loosely attached bacteria, and transferred to a sterile centrifuge tube containing 10 mL of Ringer's Solution. The coupons were then sonicated for 5 min in an ultrasonic bath to enable cellular detachment. Following sonication, serial dilutions were made to estimate the bacterial population. 0.1 mL of each dilution was then plated on TSA plates, spread evenly, and then incubated for 24–48 h (depending on the bacterial strain) at 37 °C, as per supplier instructions (Culture Collections, Public Health, England). The colonies were then enumerated as per standard counting rules. The coupon surface area was estimated to be 10.37 cm^2. Three biological replicates per coupon composition were performed for each of the four tested strains.

Statistical significance testing was performed using IBM SPSS version 28. One-way ANOVA was performed to assess for differences between Ag-containing coupons and Fe35Mn controls. Bonferroni post-hoc analysis was performed to assess differences in viable bacterial biomass counts between FeMn1Ag and FeMn5Ag. A significance level of 0.01 was adopted.

2.5. In vivo biocompatibility

In vivo tests were performed using GAERS rats after obtaining ethical approval from the Joint FREC (Faculty Research Ethics Committee) Animal Research Sectoral Sub-committee (JFARRS) at the Centre for Molecular Medicine and Biobanking, University of Malta. Anaesthesia was induced and maintained using isoflurane delivered using the SomnoSuite® (Kent Scientific®) anaesthetic system. Anaesthetised rats were operated on the SurgiSuite® (Kent Scientific®) operative platform with temperature control heating pad and each rat had an alloy pin implanted in the cancellous bone in the vertebrae at the base of the animal's tail. A total of 24 cylindrical Fe-alloy pins of FeMn, FeMn1Ag and FeMn5Ag (8 of each material) were implanted under sterile conditions. A surgical wound was created longitudinally (proximo-distally) on the left lateral side of each rat tail. An OmniDrill35 Micro Drill (World Precision Instruments, USA) was used to create a defect of similar size to the pin to be implanted. The pin was subsequently fit as tightly as possible into the defect with the length of the pin across the breadth of the vertebral body. The wounds were closed using Polypropylene sutures (SMI, Belgium) and the rats were then observed for a total period of 6 months, after which the animals were euthanised using CO$_2$ and the implants retrieved for examination.

Once euthanised all the rats' tails were removed and samples from both the region surrounding implants and also from non-implant containing vertebrae (controls), subjected to histological and corrosion analysis. The rat bodies were examined using MRI.

2.5.1. Explantation corrosion analysis

For each implanted alloy, a sample was fully removed from the implantation site following the 6-month period to identify any crystalline corrosion products using XRD and for surface imaging and elemental analysis using SEM/EDS. When carrying out XRD analysis, the same testing parameters used for sample characterisation prior to testing were used, however in this case, the samples were not rotated. For cross-sectional analysis of the implant-bone interface, a whole vertebra for each condition was embedded in cold-mounting epoxy. Once cured, the mounted bone was ground until the implanted pin was exposed, and consequently ground using SiC paper to a P2500 finish. The samples were then ultrasonicated in ethanol and dried under vacuum for further analysis.

2.5.2. Histological analysis

The part of the tail involved was sectioned longitudinally through the skin. The skin was partially removed by blunt dissection around half the circumference of the tail to allow good access of fixative and decalcification solutions to the inner tissues of the tail. Each specimen was formalin-fixed in a formalin bath for 48 h. Following this, decalcification was performed in formic acid for 2–3 weeks with regular replacement of the formic acid every 2 days. Dehydration, clearing and paraffin impregnation were performed using an automated system – the SLEE Vacuum Tissue Processor MTM-II (Halomedicals, Nigeria). Slides were then cut with a Leica RM2235 Manual Rotary Microtome (ThermoFisher Scientific ™, USA) and viewed using a ZEISS Axiostar Plus Binocular Microscope

(ThermoFisher Scientific™, USA).

3. Results

3.1. Pre-experimental characterisation of in vitro test coupons

The microstructures of the coupons were observed using SEM and are shown in Fig. 1. The microstructures of Fe and FeMn in Fig. 1a and b respectively, are clearly composed of a single phase. XRD patterns presented in Fig. 2 confirm the presence of α-ferrite and γ-austenite in Fe and FeMn respectively. Secondary electron (SE) SEM micrographs for FeMn1Ag and FeMn5Ag in Fig. 1c and d respectively, also show an additional lightly coloured phase indicating the presence of Ag. This is also reflected in the additional α-Ag phase in their XRD patterns. All microstructures also contain porosity resultant from the sintering procedure. Pore size was seldom greater than 30 μm indicating the presence of only micro-porosity and not macro-porosity. On the other hand, manganese-rich oxides like MnO [14], were not present in the microstructures following successful elimination using the described acid treatment. One should note that the superior compressibility of Fe as well as its resistance to thermal oxidation relative to Mn, results in much more dense microstructures. During testing, a higher density translates into a smaller area exposed to testing solutions.

3.2. In vitro cytotoxicity with hFOB and MC3T3 cell lines

MC3T3 cytotoxicity testing was performed to analyse any difference obtained by pre-corroding coupons versus previously uncorroded coupons. Pre-corrosion for 3 days had no effect on the luminescent signal obtained from cell viability testing with Cell-Titer-Glo® ($P = 0.999$). For this reason, corrosion was removed as a variable and subsequent analyses on MC3T3 results performed solely using luminescent signals obtained for pre-corroded coupons. The luminescent signal is proportional to the amount of ATP present, with the latter being a key biomarker indicating the presence of metabolically active cells.

Analysis of results obtained from both the hFOB and MC3T3 cell lines were first performed by way of an ANOVA model with interaction. This analysis showed a significant variation in luminescent signal obtained in relation to both the material and duration of testing ($P < 0.001$ in all cases).

Subsequent analyses were focused on the individual cell lines and the effect of the material over the test period, illustrated in Fig. 3. With regards to the hFOB cell line in Fig. 3a, luminescence was noted to decrease significantly over the 4 days of testing for FeMn1Ag
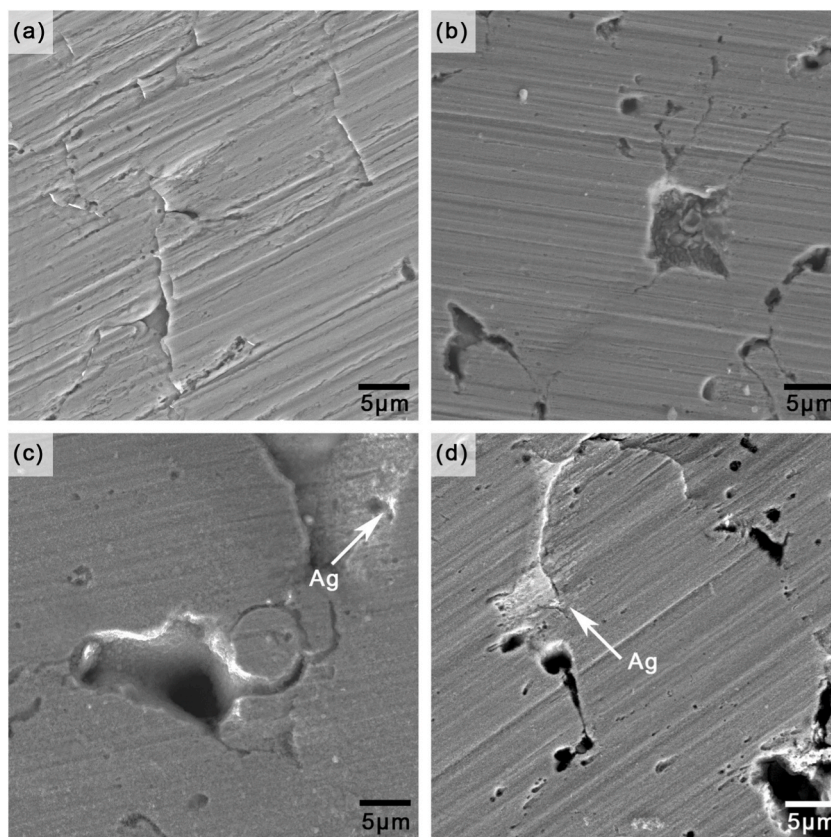

Fig. 1. SE−SEM images of (a) Fe (b) FeMn (c) FeMn1Ag and (d) FeMn5Ag ground to P2500 and acid-treated to remove MnO.
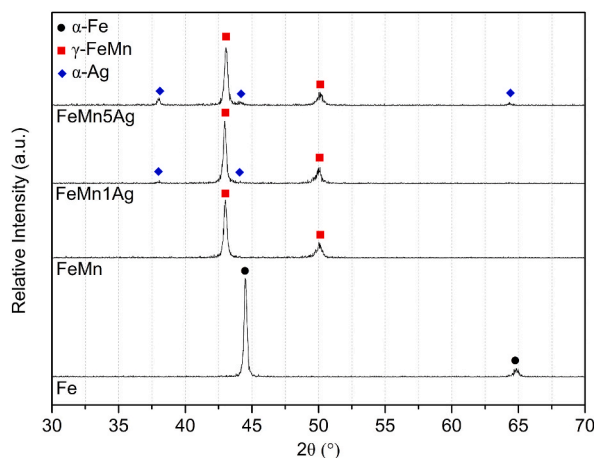
Fig. 2. XRD patterns for Fe, FeMn, FeMn1Ag and FeMn5Ag as-acid treated.

($P = 0.007$) and FeMn5Ag ($P < 0.001$), pure Fe and FeMn showing no significant difference in luminescence signals over the testing period. In contrast, Thermanox™ and SS316LVM were seen to have luminescence signals increasing significantly over the testing period of 4 days with $P = 0.005$ and $P = 0.015$ for Thermanox™ and SS316LVM respectively as shown in Fig. 3a.

MC3T3 viability was similarly poor for all of the Fe-alloy coupons as shown in Fig. 3b. None of these materials showed any significant increase in luminescence signals over the 4-day testing period for any of the test Fe-alloy coupons. This is in stark contrast to results obtained for stainless steel 316LVM which showed significantly increasing viability in the way of luminescence signals rising exponentially ($P = 0.039$).

In all test metal coupon cases for both hFOB and MC3T3 cell lines, much lower luminescence was noted as compared to both Thermanox™ and stainless steel 316LVM, in fact values barely exceeded those of medium alone without any cells. This indicates very significant cytotoxicity as assessed using the ISO10995-5:2009 standard [53].

3.3. SEM analysis of MC3T3 seeded coupons

SEM imaging of the Fe-alloy coupons clearly identified the presence of corrosion products forming on the surface of these coupons. No cells however were viewed on any of their surfaces as seen in Fig. 4(a–d). In contrast, SS316LVM clearly shows cells adherent to the surface of the coupon and cell numbers and density are noted to increase throughout the 4 days of testing, as shown in Fig. 4 (e and f).

3.4. In vitro biofilm experimentation

A graphical summary of *in vitro* biofilm results is shown in Fig. 5. There was on average a 1.32 log (CFU/cm^2) reduction in viable biomass in the Ag-containing coupons, when compared to the Ag-free controls in each of the four bacterial strains tested. These differences were statistically significant at the 0.01 level for *S. aureus* ($P < 0.001$), *S. epidermidis* ($P < 0.001$), *S. agalactiae* ($P = 0.002$), as well as *E. coli* ($P < 0.001$). A Bonferroni post-hoc analysis of the Ag-containing subgroups revealed no statistically significant difference at the 0.01 level in any of the four tested strains, indicating no significant observed difference in antibacterial activity between FeMn1Ag and FeMn5Ag coupons.

3.5. In vivo biocompatibility of FeMn, FeMn1Ag and FeMn5Ag

All 24 rats recovered uneventfully from anaesthesia and there were no events of poor wound healing, wound breakdown or infection in the post-operative period. All the rats continued to gain weight as would be expected throughout the 6-month observation period and there were no episodes of death. Upon retrieval, all the pin conditions were noted to be well fixed within the vertebral bone with no pins noted to be loose.

Magnetic resonance imaging was performed on the same day the rats were euthanised with specific sequences employed searching specifically for Fe accumulation, as would be employed in disease of Fe overload such as Haemochromatosis. No evidence of Fe accumulation was noted in any of the vital organs of any of the rats submitted to magnetic resonance imaging.

3.5.1. Histological analysis

Whilst there was no obvious corrosion attack of the metal, the bones which had been implanted with Mn-containing implants showed a clear blackening, of the surrounding bone (Fig. 6a). This included FeMn (Fig. 6a), FeMn1Ag and even FeMn5Ag (Fig. 6c). Interestingly, this colouration remained despite the Ca-depleting treatment the specimens received prior to histological processing and examination. Besides this, no other differences were noted between these specimens and control bones (Fig. 6b) which were also
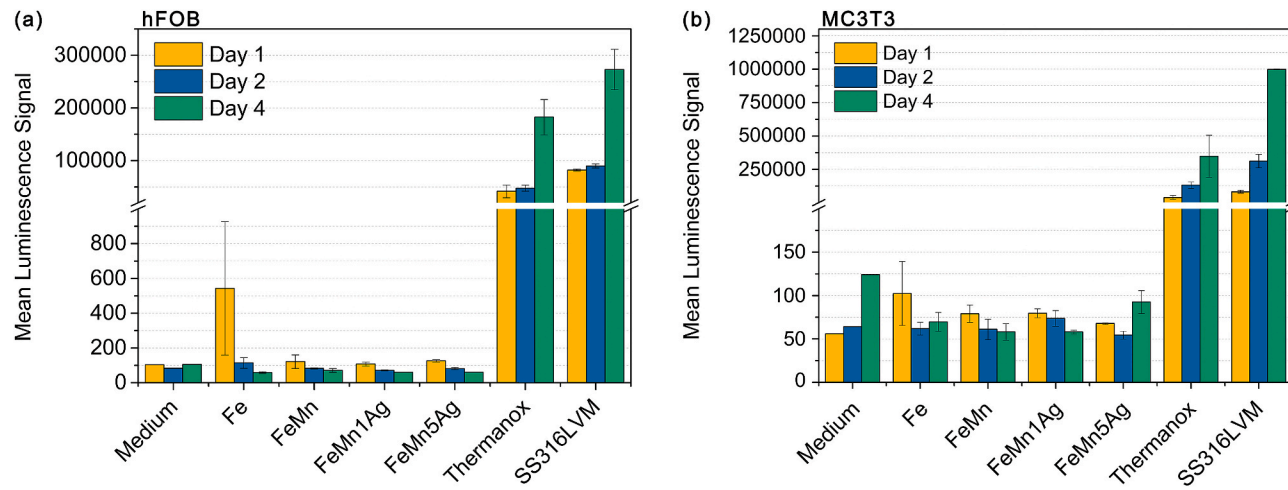
Fig. 3. Luminescence signals plotted against material over the 4 days of testing for (a) hFOB cell line on ground coupons and (b) MC3T3 cell line on pre-corroded coupons.
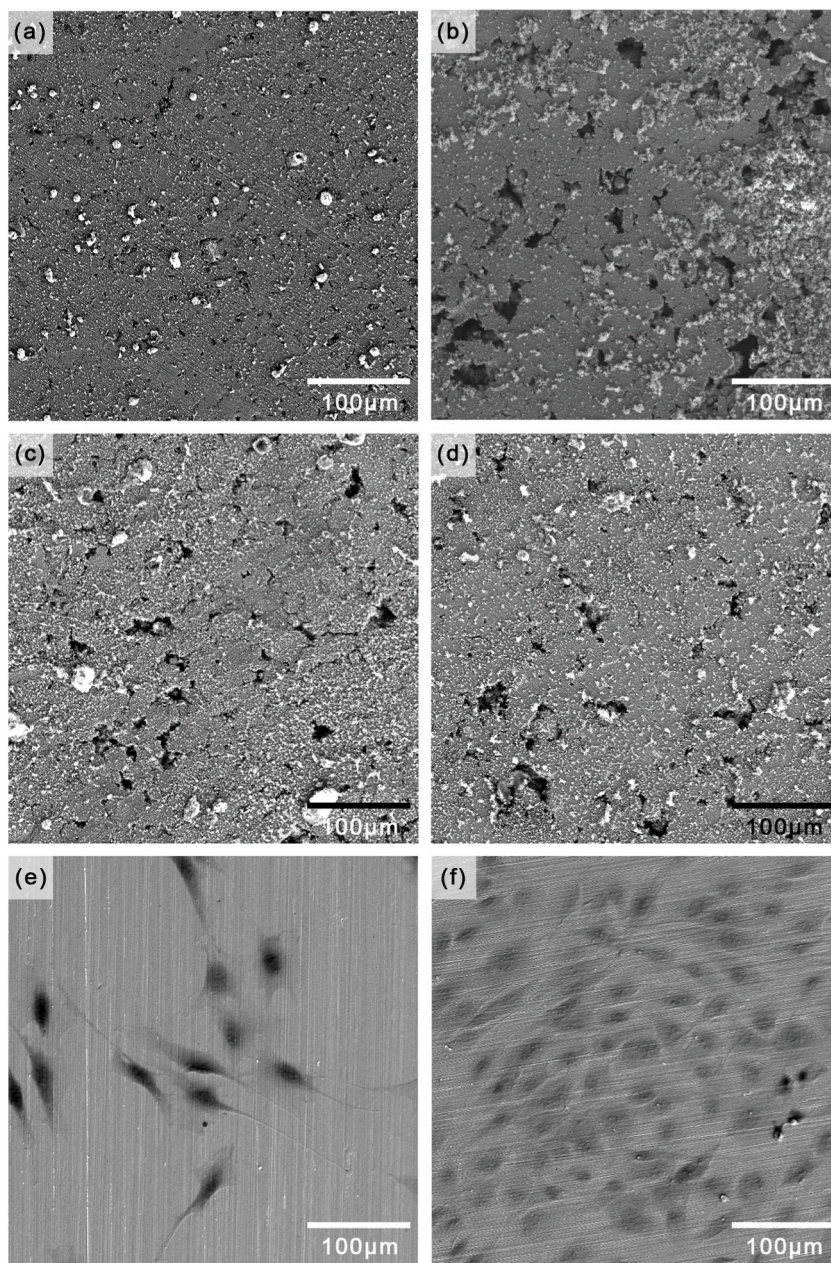
Fig. 4. Low magnification SEM images of pre-corroded coupons on day 4 of testing for (a) Fe, (b) FeMn, (c) FeMn1Ag, (d) FeMn5Ag, (e) SS316LVM on day 1, and (f) SS316LVM on day 4, following testing with MC3T3 cell line.

examined. No significant inflammatory changes were seen in any of the histological specimens with bone growing well in the region surrounding the implants.

3.5.2. Post-test characterisation of explanted pins

Explanted samples all had a similar appearance, with the surface being fully covered with a similar black product. No sign of the bare metal was visible with the naked eye indicating full coverage with corrosion product. XRD analysis of the sample surface, presented in Fig. 7, indicated that the surface product was common for all three conditions. The principal phase present matched the database patterns corresponding to $CaCO_3$. This result is promising when considering the ability of the implanted pins to integrate with the surrounding bone. The peak labelled MOOH, at around $21.4°$, corresponds to both goethite (FeOOH) and groutite (MnOOH) which have very similar crystal structures. Other very small peaks present at around $23.8°$ and $24.6°$ are more difficult to attribute to a specific phase since they could belong to any number of salts or hydroxides composed of Fe, Mn, K, Ca and P. The fact that the
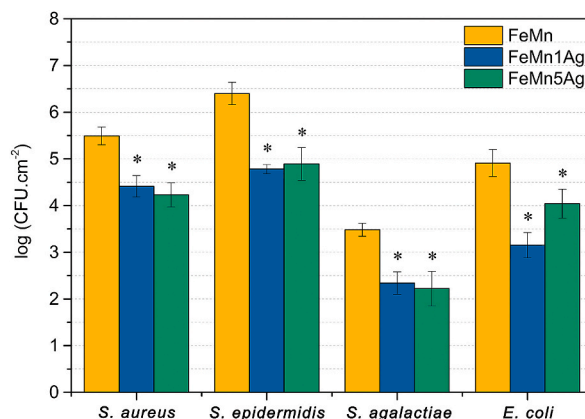
Fig. 5. Observed detached mean bacterial cell counts following incubation. * Indicates that the result is significantly different from FeMn controls at the 0.01 level of significance.

hydroxide phase peaks were present at such low relative intensities could indicate that the product was layered underneath the carbonate compound.

Fig. 8 shows the surface of (a) FeMn (b) FeMn1Ag and (c) FeMn5Ag pins following explantation, as observed using SEM. Low magnification micrographs indicate very similar surface morphologies with a very flaky corrosion product layer on top of a smoother underlying material. The cracks shown in the topmost layer could be attributed to a dehydration effect following vacuum drying the samples after ultrasonication in ethanol as a cleaning step. This may also have affected the adherence of the product to the underlying layer which resulted in flaking off in some parts as observed in Fig. 8. The compositions presented in Table 1 corresponding to the flaky layer (areas 2, 4 and 6) is consistently rich in P, Ca and O indicating some form of Ca-rich phosphate. The carbon content in general is also quite high although one must once again take note that the accuracy of carbon measurements using EDS is heavily limited. Considering the presence of $CaCO_3$ from XRD results, it is possible that the topmost layer is a mixture of both carbonate and phosphates or that it is indeed carbonate with considerable contamination of P from the surrounding bone which is predominantly made from Ca/P-like compounds. Similarly, notable amounts of K in the top layer also originate from the surrounding bone.

The underlying layers (Fig. 8, areas 1, 3 and 5), also follow similar compositional patterns despite the different alloy composition of the substrate. Whilst it is not very clear from the image whether the surface is that of the original metal or an additional corrosion layer underneath the Ca-rich material, the considerably high O content seems to indicate that there is some form of metal oxide/hydroxide present. This corroborates the result in the XRD scans in Fig. 7, where a peak at around 21.4° present in all scans indicated the detection of MOOH. Since both Fe and Mn are present, it is possible that either both groutite and goethite are present, or that a solid solution of both, or similar hydroxides, is present.

Cross-sectional analysis of the pins indicated that the corrosion product layer, although seemingly present all over the pin circumference, varied significantly in thickness from one spot to another. However, the corrosion product observed at the metal-corrosion product interface of the FeMn5Ag implant, was consistently thicker than that formed on FeMn and FeMn1Ag, at instances reaching a thickness of around 30 μm. Fig. 8d, e and f show a sample section from each implant, with corresponding EDS analysis presented in Table 1. EDS analysis continued to confirm that, in general, the corrosion product composition was unaffected by the alloy composition.

One must note that cracks in the corrosion product, as explained already, could be due to the sample preparation method. Both vacuum-drying as well as cold-mounting in epoxy could have encouraged corrosion product flaking and separation, as observed in Fig. 8f.

Fig. 9a shows an FeMn1Ag pin surface filled with micro-voids prior to *in vivo* testing. The image contrasts with the micrograph in Fig. 9b which shows a cross-section of the same material following testing along with corresponding EDS mapping. The maps show how material from the products and surrounding bone are intermixed with epoxy whereas the micro-voids shown in Fig. 9a were completely filled with metal oxides, without extensive degradation propagating through the sample's internal structure. The maps also clearly indicate that the first layer in contact with the pin surface is mainly composed of metal oxides with hints of P and Ca being present only further towards the bone.

4. Discussion

4.1. Cytotoxicity and biocompatibility

Cytotoxicity in our work was evaluated through the use of direct cytotoxicity techniques, a valid testing method described in ISO10993-5:2009 standard [53]. All tests showed Fe-alloy test materials to be significantly cytotoxic with apparently no surviving cells adherent to their surfaces by the end of the fourth day of testing. Pre-corrosion did not have any bearing of the viability of seeded cells either, with all pre-corroded coupons giving luminescence signals similar to those obtained from previously uncorroded coupons. This
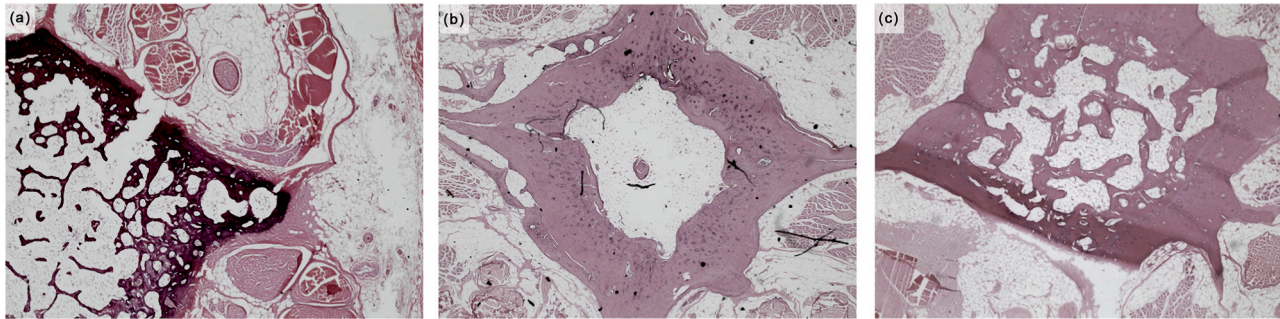
Fig. 6. Haematoxylin and Eosin-stained histological specimens prepared from rat tails. (a) Shows a highlight of the vertebral body of a rat tail showing bone which has been extensively blackened by a FeMn implant, (b) shows a vertebra from a control rat with no implant where normal collagen matrix colouration for decalcified bone is appreciated and (c) shows bone surrounding an area FeMn5Ag pin was implanted.
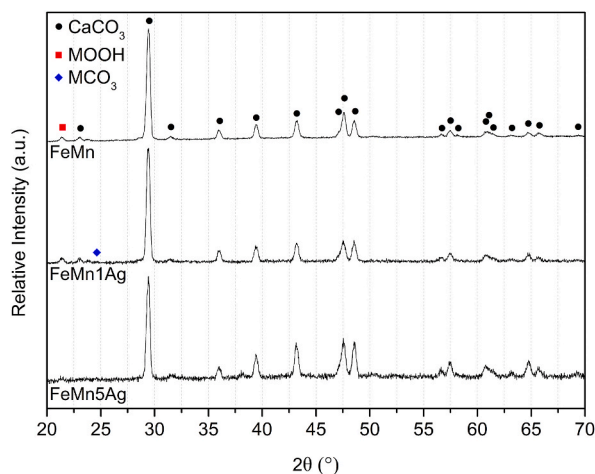
Fig. 7. XRD patterns for the surfaces of FeMn, FeMn1Ag and FeMn5Ag pins following a 6-month implantation period.

is in stark contrast to the results obtained for both stainless steel 316LVM and Thermanox™, both of which allowed unhindered growth of cell lines on their surfaces.

Much work has thus far been performed using indirect techniques where cells are grown in medium where the material has previously been corroding. In the authors' view however, this methodology fails to replicate some of the key factors of eventual *in vivo* use. Being exposed only to soluble components derived from the material fails to replicate the dynamic environment to which *in vivo* cells are exposed, also in direct contact with the metal or its insoluble derivatives.

With both pre-corroded and uncorroded coupons, no significant difference in cytotoxicity and resultant cell viability was noted between the two, this is believed to stem from two issues. The first is the volume of cytotoxic material the cells are exposed to. While other works have reported acceptable cytotoxicity profiles [26,54], Scarcello *et al.* [55,56], report on the formation of hydroxyl radicals and the resultant oxidative stress in cells directly exposed to Fe-based materials. In their work, cells exposed to these materials directly, were negatively impacted in a dose-dependent manner. With the addition of catalase which decreases the formation of hydroxyl radicals however, this cytotoxic effect was seen to decrease significantly. The same was also true for those cells exposed indirectly to the same materials [55,56]. In addition, the utilised samples' structure in the work by Scarcello *et al.* [55], exhibited only microporosity of <50 μm. The eventual implant would necessarily be osteoconductive optimally, at macroporosities in the region of 150–300 μm instead [57]. Along with the necessity of pore interconnectivity, this would greatly increase the surface area available for corrosion, increasing corrosion product formation rate and negatively impacting surrounding cells' viability.

The second issue is that of flaking of corrosion products seen in the *in vitro* environment as seen in Fig. 8c. Here, corrosion products forming on the surface of implants may occasionally flake off. This decreases cell adherence to the surface of the coupon but also exposes previously uncorroded material to readily available, dissolved O_2 [14,29], re-accelerating corrosion and the potential for production of cytotoxic ionic material. Considering that an implant positioned *in vivo* is necessarily surrounded by bone and/or soft tissue, this situation is unlikely to be replicated in an *in vivo* situation. In the latter environment, flakes of corrosion products are less likely to be flushed away by any physiological fluids and would instead accumulate at the sample surface creating a physical barrier between the implant and the extracellular environment [26,29]. Being relatively insoluble [58], unlike magnesium oxide which may form hydroxide and become more soluble and thus more easily removed, this might also explain the little corrosion and favourable cytotoxicity profile seen after 6 months of *in vivo* implantation (Fig. 9b) seen here but also reported by other groups [54,59]. The lack of obvious Fe deposition seen within the vital organs on MRI also supports this.

SE−SEM imaging of the explanted pins used *in vivo* in Fig. 8a to c, confirm this suspicion of a barrier layer forming between the implant and the exterior extracellular environment [60]. Although a flaky layer was seen to form on the surface of the explanted pins, flaking most likely took place in the sample preparation stage during vacuum drying, and the layer was intact *in vivo*. Cross-sectional imaging in Fig. 8d to f clearly defines a variable thickness corrosion layer forming on the exterior surface of the pins with oxide product only forming within voids of the implant, the majority of the implant being left intact and uncorroded. Of the three materials, FeMn5Ag exhibited the thickest corrosion product layer *in vivo*, as shown in Fig. 8f. Although this seems to confirm the numerous counts of successful *in vitro* corrosion acceleration with the incorporation of Ag [15,16,30,31,43,60], the accelerated corrosion effect could still have been limited to the first weeks following implantation; a hypothesis that is supported by the authors' previous work on localised *in vitro* corrosion analysis in close proximity to the corroding surfaces of Fe, FeMn and FeMn5Ag [14]. In that study, as opposed to Ag-free materials, the degradation of FeMnAg became strongly diffusion limited as the strong initial microgalvanic reaction depleted the surrounding electrolyte from dissolved oxygen necessary to sustain the dominant cathodic reaction at physiological conditions [14, 29]. In fact, Dargusch *et al.* [31] noted that the corrosion rate dropped by half between the fourth and twelfth week for both Fe35Mn and Fe35Mn1Ag pins implanted subcutaneously, despite a relatively fast initial corrosion rate. This uncommonly fast corrosion rate *in vivo* might have been affected by the implantation site, as when adopting a similar microgalvanic acceleration approach with FeMnPd alloys implanted in femurs, Kraus *et al.* [32] barely observed any degradation. Kraus *et al.* also observed very little changes in
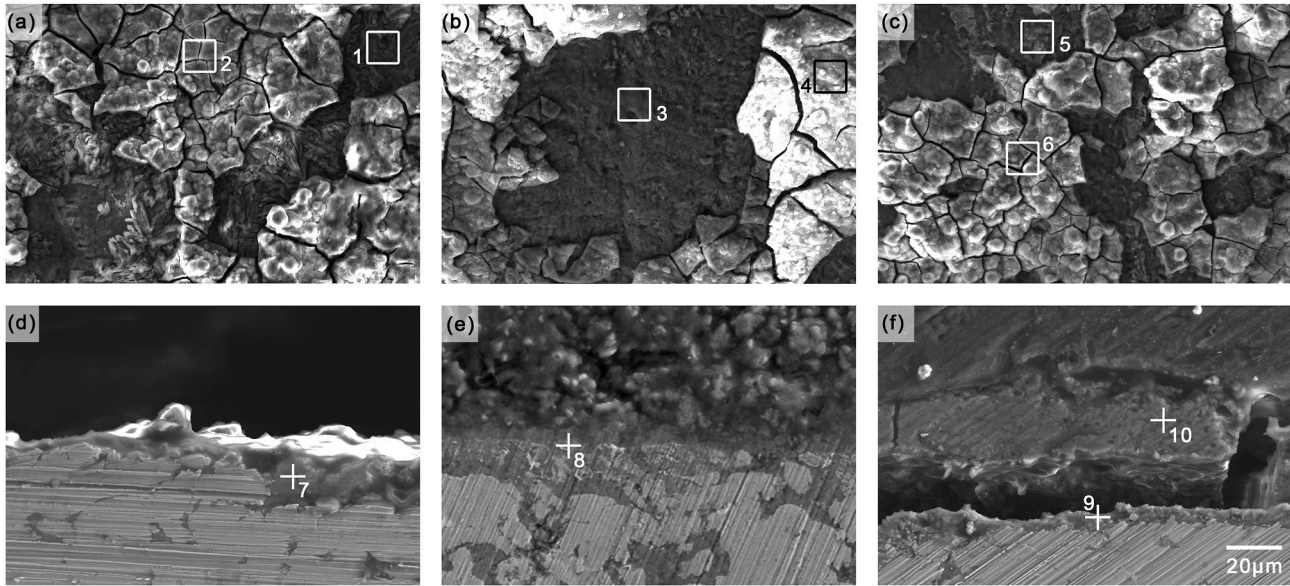
Fig. 8. SE−SEM images of explanted (a) FeMn, (b) FeMn1Ag and (c) FeMn5Ag pins following a 6-month implantation period. Cross-sectional images of explanted (d) FeMn, (e) FeMn1Ag and (f) FeMn5Ag pins at the metal-corrosion product interface. Boxes and crosses marked with numbers 1 to 6 and 7 to 10 respectively indicate areas or spots where EDS analysis was performed. Results of the analysis are given in Table 1.

Table 1

EDS analysis corresponding to regions of interest specified in Fig. 8. Numbers 1 to 6 are area EDS while numbers 7 to 10 are spot EDS.

Element wt. %	1	2	3	4	5	6	7	8	9	10
C	28.08	17.13	25.48	30.81	17.58	18.60	30.18	29.19	35.82	41.02
N	6.10	3.89	6.02	4.30	4.61	4.23	–	–	–	–
O	35.65	42.37	33.96	28.47	44.81	40.15	30.29	28.89	28.78	29.53
Na	0.30	1.12	0.81	0.97	0.62	1.30	0.53	–	0.38	0.86
P	1.35	8.48	3.59	6.98	1.28	7.90	7.17	7.40	1.98	4.63
S	1.57	0.31	2.07	0.47	0.80	0.57	–	–	–	–
K	0.12	1.04	0.15	1.33	0.12	1.47	0.59	1.06	0.31	1.05
Ca	0.56	3.60	0.44	2.81	0.15	3.10	1.23	2.86	0.33	2.09
Mn	8.05	2.17	6.29	1.71	9.53	1.53	5.76	5.14	1.49	1.34
Fe	18.22	19.89	21.19	22.15	20.50	21.15	24.25	25.47	30.92	19.48
Ag	–	–	–	–	–	–	–	–	–	–

accumulated corrosion product between 4 and 52 weeks due to limited dissolved oxygen availability. This lends support to the thought that while FeMn5Ag could allow for faster degradation rates, considerable degradation could only be achieved by increased surface-to-volume ratios and possibly by flushing away of corrosion products as they are formed – an event that is not particularly likely in most orthopaedic implantation sites, especially when considering insoluble corrosion products. This would naturally put greater weight on the careful review of mechanical performance analysis of corroded samples to ensure that the mechanical integrity of the implant is not compromised early on in this process.

In vivo pins were macroscopically well-fixed within bone at the end of the 6-month test period. Histological analysis in Fig. 6 confirmed the presence of bone formation at and around the bone-implant interface with the only visible effect being the blackening of tissues surrounding the implant, as may occur in bone exposed to oxides of Fe and particularly of Mn [61]. Mn-oxides are well known to cause the mineral-induced blackening of skeletal remains [62]. Mn had been shown to accumulate heavily in rat bone after oral administration with significant accumulation of Mn in bone occurring after 4 weeks of chronic oral exposure in rats in previous studies. Once Mn administration was stopped, an average half-life of the bone-bound Mn of 170 days was recorded [63]. EDS and XRD analysis also showed the presence of compounds such as $CaCO_3$ and various hydroxides, which are likely to be due to formation and attachment of bone on the implant/corrosion product surface. Traverson *et al.* [59] commented on the histological appearance at the bone-implant interface of FeMn implanted *in vivo*. In their analysis, FeMn may have acted as a mild local irritant, our results concurring with their observance of *in vivo* bone growth onto the implant with no visible inflammatory changes however noted in our work. Other work corroborates these findings [9,31,64] but some evidence such as that reported by Wegener *et al.* [65] may suggest that long-term implantation of Fe-based implants may cause accumulation of Fe deposits in tissues such as regional lymph nodes in addition to raised levels of serum Fe and ferritin. It is noteworthy that the implant under study by Wegener *et al.* [65] was of much greater porosity and of different composition to that under study in our work and therefore it is unlikely to be used in a load-bearing orthopaedic application.

4.2. Antibacterial activity

Ag has long been known to possess antibacterial activity. In fact, it was the most important antibacterial agent of the pre-antibiotic era [66]. From the observed results, it is evident that the addition of Ag to Fe35Mn coupons brings about a statistically significant, broad-spectrum biofilm-retardant effect. Furthermore, as may be seen in Fig. 5, there appears to be no added anti-biofilm benefit derived from FeMn5Ag in comparison to FeMn1Ag. This could perhaps indicate that a maximal dose response was already achieved with FeMn1Ag, and may suggest that a similar effect could also be brought about with an even smaller amount of Ag. The implications of these findings are twofold: firstly, that a lower exposure to Ag and its cumulative adverse effects is possible without compromising on antibacterial activity, and secondly, that effective antibacterial activity may be produced at a more competitive cost.

These results jar somewhat with the existing, albeit scant, literature pertaining to FeMnAg alloys and their antibacterial resistance. Despite noting a strong antibacterial effect in Ag-containing alloys when compared to controls, Sotoudehbagha *et al.* [44] observed greater overall antibacterial rates with (Fe30Mn)3Ag when compared to (Fe30Mn)1Ag. On the contrary, Liu *et al.* [43] noted no observable antibacterial effect in Ag-containing iron-manganese alloys following 24 h of incubation. The authors attributed this to a paucity of leached Ag^+ ions into the surrounding bacterial solution. It is worthwhile noting that in the work by Liu *et al.*, bacterial exposure to the Ag-containing and Ag-free coupons occurred for just 4 h, following which a volume of the exposed bacterial suspension was added to well plates containing TSB, and incubated for a further 24 h away from the coupons. Bacterial cell growth was then estimated continuously using time-dependent optical densitometry. The observed lack of antibacterial activity in the Ag-containing coupons could have therefore been the result of a limited exposure time.

A direct comparison of results may however be counterproductive; the methodology used in both studies differs greatly from that used in this work [43,44]. Firstly, both studies investigate the effects of exposing largely planktonic populations of bacteria to alloyed Ag. On the other hand, in the current study the bacterial biofilm attached to the alloyed coupons was quantified, a parameter that could potentially be of greater clinical importance should the alloy be implanted into living subjects. Secondly, both studies investigate the antibacterial activity of alloyed Ag against *Staphylococcus* aureus and *Escherichia coli* [43,44]. This experiment, whilst including the latter two species, also considers the antibacterial effects of alloyed Ag against coagulase-negative *Staphyloccocci* as well as Lancefield
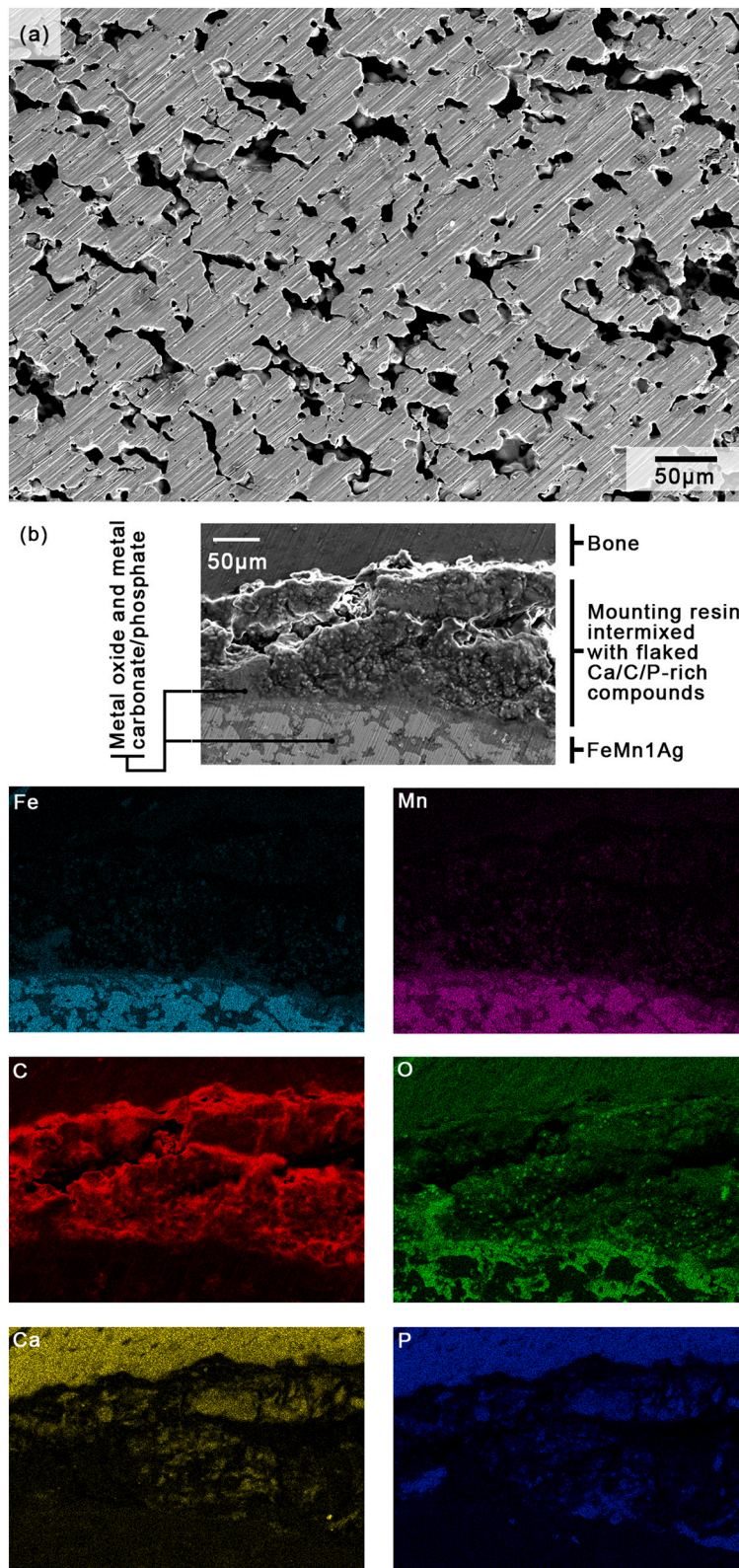
Fig. 9. (a) FeMn1Ag as-acid treated prior to *in vivo* test and (b) labelled FeMn1Ag following explantation and EDS analysis. Maps represent Fe, Mn, C, O, Ca and P distribution corresponding to (b).

Group B *Streptococci*. These four bacterial species are implicated in nearly three quarters of all prosthetic joint infections [45] and fracture-related infections [46]. This work therefore provides a more comprehensive understanding of the potential antibacterial effects of Ag-containing, biodegradable, iron-manganese alloys in the clinical context, and is, to the best of our knowledge, the first of its kind.

It must be said, however, that the observed antibacterial activity may not be directly due to the antibacterial activity of Ag. Mn has also been noted to possess antibacterial effects [67,68]. Naturally, one would therefore be inclined to question as to how the difference in bacterial counts between the Ag-containing coupons and the Ag-free controls obtained in this experiment arose. It is plausible that the initially accelerated corrosion potentiated by Ag-rich sites within the Ag-containing alloys, as observed in multiple *in vitro* corrosion tests in various physiological media [14,29], increased the elution of bactericidal Mn corrosion products into the culture medium, thereby reducing the population of planktonic bacteria available for attachment and biofilm propagation.

5. Conclusion

Thus far, a rift between *in vitro* and *in vivo* experimentation exists. A complete explanation of the reasons for this has so far been elusive, with differences in results being evident. Surely, the complexities of an *in vivo* environment, including a dynamic environment, blood stream and fresh availability of bone cell progenitors [69,70] is a strong factor adding to the complexity of this problem.

Considering the findings of this work amongst the available evidence, FeMn and FeMnAg alloys still exhibit some limitations for use in orthopaedic application with regards to their corrosion performance and cytocompatibility. They do however continue to show promise in orthopaedics. The authors suggest further *in vivo* work using a large animal model that would allow implantation of FeMnAg in the form of a porous scaffold. This would hypothetically allow for high mass loss along with *in vitro* proven infection-resistance.

Author contribution statement

Luke Saliba, Keith Sammut, Christabelle Tonna: Performed the experiments; Analyzed and interpreted the data; Wrote the paper.
Foteini Pavli: Conceived and designed the experiments; Wrote the paper.
Vasilis Valdramidis: Conceived and designed the experiments; Contributed reagents, materials, analysis tools or data; Wrote the paper.
Ray Gatt, Ryan Giordmaina: Contributed reagents, materials, analysis tools or data; Wrote the paper.
Liberato Camilleri: Analyzed and interpreted the data.
William Atanasio: Performed the experiments; Analyzed and interpreted the data; Contributed reagents, materials, analysis tools or data.
Joseph Buhagiar: Conceived and designed the experiments; Analyzed and interpreted the data; Contributed reagents, materials, analysis tools or data; Wrote the paper.
Pierre Schembri Wismayer: Conceived and designed the experiments; Performed the experiments; Analyzed and interpreted the data; Contributed reagents, materials, analysis tools or data; Wrote the paper.

Data availability statement

Data will be made available on request.

Declaration of competing interest

The authors declare that they have no competing interests.

Acknowledgements

References

[1] C.G. Finkemeier, Bone-grafting and bone-graft substitutes, J. Bone Joint Surg. 84 (3) (2002) 454–464.
[2] C. Laurencin, Y. Khan, S.F. El-Amin, Bone graft substitutes, Expet Rev. Med. Dev. 3 (1) (2006) 49–57.
[3] C.E. Gillman, A.C. Jayasuriya, FDA-approved bone grafts and bone graft substitute devices in bone regeneration, Mater. biol. Appl. 130 (2021), 112466.
[4] M. Heiden, E. Walker, L. Stanciu, Magnesium, iron and zinc alloys, the trifecta of bioresorbable orthopaedic and vascular implantation - a review, J. Biotechnol. Biomater. 5 (2015) 178.
[5] L. Li, et al., Corrosion and biocompatibility improvement of magnesium-based alloys as bone implant materials: a review, Regen. Biomater. 4 (2) (2017) 129–137.
[6] C. Liu, et al., Biodegradable magnesium alloys developed as bone repair materials: a review, Scanning (2018), 9216314.
[7] M. Peuster, et al., Long-term biocompatibility of a corrodible peripheral iron stent in the porcine descending aorta, Biomaterials 27 (28) (2006) 4955–4962.
[8] R. Waksman, et al., Short-term effects of biocorrodible iron stents in porcine coronary arteries, J. Intervent. Cardiol. 21 1 (2008) 15–20.
[9] B. Wegener, et al., Development of a novel biodegradable porous iron-based implant for bone replacement, Sci. Rep. 10 (1) (2020) 9141.
[10] T.C. Paim, et al., Evaluation of in vitro and in vivo biocompatibility of iron produced by powder metallurgy, Mater. Sci. Eng. C 115 (2020), 111129.

[11] M. Peuster, et al., A novel approach to temporary stenting: degradable cardiovascular stents produced from corrodible metal-results 6-18 months after implantation into New Zealand white rabbits, Heart (British Cardiac Society) 86 (5) (2001) 563–569.

[12] H. Hermawan, D. Dubé, D. Mantovani, Degradable metallic biomaterials: design and development of Fe–Mn alloys for stents, J. Biomed. Mater. Res. 93A (1) (2010) 1–11.

[13] J. Čapek, et al., Microstructural, mechanical, corrosion and cytotoxicity characterization of the hot forged FeMn30(wt.%) alloy, Mater. Sci. Eng. C 58 (2016) 900–908.

[14] C. Tonna, et al., Biodegradation behaviour of Fe-based alloys in Hanks' Balanced Salt Solutions: Part I. material characterisation and corrosion testing, Bioact. Mater. 7 (2022) 426–440.

[15] M. Wiesener, et al., Corrosion properties of bioresorbable FeMn-Ag alloys prepared by selective laser melting, Mater. Corros. 68 (10) (2017) 1028–1036.

[16] P. Sotoudeh Bagha, et al., Design and characterization of nano and bimodal structured biodegradable Fe-Mn-Ag alloy with accelerated corrosion rate, J. Alloys Compd. 767 (2018) 955–965.

[17] H. Hermawan, et al., Iron–manganese: new class of metallic degradable biomaterials prepared by powder metallurgy, Powder Metall. 51 (1) (2008) 38–45.

[18] M.S. Dargusch, et al., Exploring the role of manganese on the microstructure, mechanical properties, biodegradability, and biocompatibility of porous iron-based scaffolds, ACS Biomater. Sci. Eng. 5 (4) (2019) 1686–1702.

[19] M. Dehestani, et al., Effects of microstructure and heat treatment on mechanical properties and corrosion behavior of powder metallurgy derived Fe–30Mn alloy, Mater. Sci. Eng., A 703 (2017) 214–226.

[20] C. Shuai, et al., Selective laser melted Fe-Mn bone scaffold: microstructure, corrosion behavior and cell response, Mater. Res. Express 7 (1) (2020), 015404.

[21] K.J. Horning, et al., Manganese is essential for neuronal health, Annu. Rev. Nutr. 35 (2015) 71–108.

[22] J. Crossgrove, W. Zheng, Manganese toxicity upon overexposure, NMR Biomed. 17 (8) (2004) 544–553.

[23] B. Liu, Y.F. Zheng, Effects of alloying elements (Mn, Co, Al, W, Sn, B, C and S) on biodegradability and in vitro biocompatibility of pure iron, Acta Biomater. 7 (3) (2011) 1407–1420.

[24] S. Mandal, et al., In vitro and in vivo degradability, biocompatibility and antimicrobial characteristics of Cu added iron-manganese alloy, J. Mater. Sci. Technol. 84 (2021) 159–172.

[25] H. Hermawan, et al., Fe-Mn alloys for metallic biodegradable stents: degradation and cell viability studies, Acta Biomater. 6 (5) (2010) 1852–1860.

[26] Y. Nie, et al., In vitro and 48 weeks in vivo performances of 3D printed porous Fe-30Mn biodegradable scaffolds, Acta Biomater. 121 (2021) 724–740.

[27] B. Paul, et al., Cell–material interactions in direct contact culture of endothelial cells on biodegradable iron-based stents fabricated by laser powder bed fusion and impact of ion release, ACS Appl. Mater. Interfaces 14 (1) (2022) 439–451.

[28] M. Schinhammer, et al., Design strategy for biodegradable Fe-based alloys for medical applications, Acta Biomater. 6 (5) (2010) 1705–1713.

[29] C. Wang, et al., Biodegradation behaviour of Fe-based alloys in Hanks' Balanced Salt Solutions: Part II. The evolution of local pH and dissolved oxygen concentration at metal interface, Bioact. Mater. 7 (2022) 412–425.

[30] M. Caligari Conti, et al., The effect of alloying elements on the properties of pressed and non-pressed biodegradable Fe–Mn–Ag powder metallurgy alloys, Heliyon 5 (9) (2019), e02522.

[31] M.S. Dargusch, et al., In vivo evaluation of bioabsorbable Fe-35Mn-1Ag: first reports on in vivo hydrogen gas evolution in Fe-based implants, Advanced Healthcare Materials 10 (2) (2021), 2000667.

[32] T. Kraus, et al., Biodegradable Fe-based alloys for use in osteosynthesis: outcome of an in vivo study after 52 weeks, Acta Biomater 10 (7) (2014) 3346–3353.

[33] M. Kostakioti, M. Hadjifrangiskou, S.J. Hultgren, Bacterial biofilms: development, dispersal, and therapeutic strategies in the dawn of the postantibiotic era, Cold Spring Harbor perspectives in medicine 3 (4) (2013) a010306.

[34] C.D. Nadell, et al., Extracellular matrix structure governs invasion resistance in bacterial biofilms, ISME J. 9 (8) (2015) 1700–1709.

[35] R.O. Darouiche, Treatment of infections associated with surgical implants, N. Engl. J. Med. 350 (14) (2004) 1422–1429.

[36] E. Alp, et al., Incidence and economic burden of prosthetic joint infections in a university hospital: a report from a middle-income country, Journal of infection and public health 9 (4) (2016) 494–498.

[37] V. Boddapati, et al., Revision total knee arthroplasty for periprosthetic joint infection is associated with increased postoperative morbidity and mortality relative to noninfectious revisions, J. Arthroplasty 33 (2) (2018) 521–526.

[38] B. Kubista, et al., Reinfection after two-stage revision for periprosthetic infection of total knee arthroplasty, Int. Orthop. 36 (1) (2012) 65–71.

[39] J. Bongers, et al., Reinfection and re-revision rates of 113 two-stage revisions in infected TKA, Journal of Bone and Joint Infection 5 (3) (2020) 137–144.

[40] A.R. Cochran, et al., Risk of reinfection after treatment of infected total knee arthroplasty, J. Arthroplasty 31 (9) (2016) 156–161.

[41] S.M. Mortazavi, et al., Revision total knee arthroplasty infection: incidence and predictors, Clin. Orthop. Relat. Res. 468 (8) (2010) 2052–2059.

[42] G. Tokmaji, et al., Silver-coated endotracheal tubes for prevention of ventilator-associated pneumonia in critically ill patients, Cochrane Database Syst. Rev. 8 (2015) CD009201.

[43] R.-Y. Liu, et al., Design of Fe–Mn–Ag alloys as potential candidates for biodegradable metals, Acta Metall. Sin. 31 (6) (2018) 584–590.

[44] P. Sotoudehbagha, et al., Novel antibacterial biodegradable Fe-Mn-Ag alloys produced by mechanical alloying, Mater. Sci. Eng. C 88 (2018) 88–94.

[45] A.J. Tande, R. Patel, Prosthetic joint infection, Clin. Microbiol. Rev. 27 (2) (2014) 302–345.

[46] M. Depypere, et al., Pathogenesis and management of fracture-related infection, Clin. Microbiol. Infection 26 (5) (2020) 572–578.

[47] P.L. Drake, K.J. Hazelwood, Exposure-related health effects of silver and silver compounds: a review, Ann. Occup. Hyg. 49 (7) (2005) 575–585.

[48] N. Hadrup, A.K. Sharma, K. Loeschner, Toxicity of silver ions, metallic silver, and silver nanoparticle materials after in vivo dermal and mucosal surface exposure: a review, Regul. Toxicol. Pharmacol. 98 (2018) 257–267.

[49] C. Recordati, et al., Tissue distribution and acute toxicity of silver after single intravenous administration in mice: nano-specific and size-dependent effects, Part. Fibre Toxicol. 13 (12) (2015).

[50] World Health Organisation. Silver in Drinking Water: Background Document for Development of WHO Guidelines for Drinking-Water Quality, World Health Organization, 2021.

[51] S. Loffredo, et al., Six-month long in vitro degradation tests of biodegradable twinning-induced plasticity steels alloyed with Ag for stent applications, ACS Biomater. Sci. Eng. 7 (8) (2021) 3669–3682.

[52] N.E. Putra, et al., Extrusion-based 3D printing of ex situ-alloyed highly biodegradable MRI-friendly porous iron-manganese scaffolds, Acta Biomater. 134 (2021) 774–790.

[53] International Organization for Standardization. ISO 10993-5:2009 Biological Evaluation of Medical Devices — Part 5: Tests for *in vitro* cytotoxicity, 2009.

[54] A. Drynda, et al., In vitro and in vivo corrosion properties of new iron–manganese alloys designed for cardiovascular applications, J. Biomed. Mater. Res. B Appl. Biomater. 103 (3) (2015) 649–660.

[55] E. Scarcello, et al., Hydroxyl radicals and oxidative stress: the dark side of Fe corrosion, Colloids Surf. B Biointerfaces 185 (2020), 110542.

[56] E. Scarcello, D. Lison, Are Fe-based stenting materials biocompatible? A critical review of *in vitro* and *in vivo* studies, J. Funct. Biomater. 11 (1) (2020).

[57] B.-S. Chang, et al., Osteoconduction at porous hydroxyapatite with various pore configurations, Biomaterials 21 (12) (2000) 1291–1298.

[58] J. Cheng, et al., Comparative in vitro study on pure metals (Fe, Mn, Mg, Zn and W) as biodegradable metals, J. Mater. Sci. Technol. 29 (7) (2013) 619–627.

[59] M. Traverson, et al., In vivo evaluation of biodegradability and biocompatibility of Fe30Mn alloy, Vet. Comp. Orthop. Traumatol. 31 (1) (2018) 10–16.

[60] N. Babacan, et al., Effect of silver additions on the microstructure, mechanical properties and corrosion behavior of biodegradable Fe-30Mn-6Si, Mater. Today Commun. 28 (2021), 102689.

[61] E. Stathopoulou, T. Theodoropoulou, N. Phoca-Cosmetatou, Black fish bones in waterlogged deposits: the case of the Neolithic lake settlement of Dispilio, Greece, Archaeofauna (22) (2013) 51–74.

[62] A.B. Marín Arroyo, et al., Archaeological implications of human-derived manganese coatings: a study of blackened bones in El Mirón Cave, Cantabrian Spain, J. Archaeol. Sci. 35 (3) (2008) 801–813.

[63] S.L. O'Neal, et al., Manganese accumulation in bone following chronic exposure in rats: steady-state concentration and half-life in bone, Toxicol. Lett. 229 (1) (2014) 93–100.

[64] D. Carluccio, et al., Additively manufactured iron-manganese for biodegradable porous load-bearing bone scaffold applications, Acta Biomater. 103 (2020) 346–360.

[65] B. Wegener, et al., Local and systemic inflammation after implantation of a novel iron based porous degradable bone replacement material in sheep model, Sci. Rep. 11 (1) (2021), 12035.

[66] J.W. Alexander, History of the medical use of silver, Surg. Infect. 10 (3) (2009) 289–292.

[67] K. Rekha, et al., Structural, optical, photocatalytic and antibacterial activity of zinc oxide and manganese doped zinc oxide nanoparticles, Phys. B Condens. Matter 405 (15) (2010) 3180–3185.

[68] N. Sharma, et al., Synthesis, characterisation and antimicrobial activity of manganese-and iron-doped zinc oxide nanoparticles, J. Exp. Nanosci. 11 (1) (2016) 54–71.

[69] H. Schell, et al., The haematoma and its role in bone healing, Journal of experimental orthopaedics 4 (1) (2017) 1–11.

[70] E. Gibon, L. Lu, S.B. Goodman, Aging, inflammation, stem cells, and bone healing, Stem Cell Res. Ther. 7 (1) (2016) 44.